THE JOURNAL OF PHYSICAL CHEMISTRY B

pubs.acs.org/JPCB Article

Proton Transfer Dynamics in the Aprotic Proton Accepting Solvent 1-Methylimidazole

Joseph E. Thomaz,[§] Alice R. Walker,[§] Stephen J. Van Wyck, Jan Meisner, Todd J. Martinez, and Michael D. Fayer*

Cite This: J. Phys. Chem. B 2020, 124, 7897−7908 Read Online

ACCESS | Metrics & More | Article Recommendations | Supporting Information

ABSTRACT: The dynamics of proton transfer to the aprotic solvent 1-methylimidazole (MeIm, proton acceptor) from the photoacid 8-hydroxypyrene-1,3,6-trisulfonic acid trisodium salt (HPTS) was investigated using fast fluorescence measurements. The closely related molecule, 8-methoxypyrene-1,3,6-trisulfonic acid trisodium salt (MPTS), which is not a photoacid, was also studied for comparison. Following optical excitation, the wavelength-dependent population dynamics of HPTS in MeIm resulting from the deprotonation process were collected over the entire fluorescence emission window. Analysis of the time-dependent fluorescence spectra revealed four distinct fluorescence bands that appear and decay on different time scales. We label these four states as protonated (P), associated I (A_I), associated II (A_{II}), and deprotonated (D). We find that the simple kinetic scheme of P → A_I → A_{II} → D is not consistent with the data. Instead, the kinetic scheme that describes the data has P decaying into A_I, which mainly goes on to deprotonation (D), but A_I can also feed into A_{II}. A_{II} can return to A_I or decay to the ground state, but does not deprotonate within experimental error. Quantum chemistry and excited state QM/MM Born−Oppenheimer molecular dynamics simulations indicate that A_I and A_{II} are two H-bonding conformations of MeIm to the HPTS hydroxyl, axial, and equatorial, respectively.

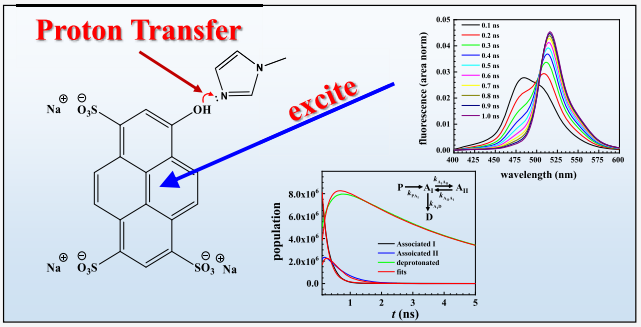

1. INTRODUCTION

The study of proton transport in nonaqueous liquids is of intrinsic interest and is important in areas ranging from biology to energy applications. For example, nonaqueous proton transfer in organic liquids may have applications in fuel cells. Currently, most common proton exchange membrane fuel cells are unable to operate at desirably high temperatures because of the volatility of water.[1] Typically, such fuel cells operate at 80 °C.[2] Thermally stable high boiling point organic solvents capable of efficient proton transport could be useful for increasing the operation temperature.

Proton transfer in a bulk liquid has been studied extensively in water.[3−9] Photoacids provide a particularly useful approach to probe proton dynamics over a wide range of time scales.[5,7,10−13] A photoacid is an alcohol or an amine in its ground electronic state. Upon optical excitation, the pK_a of the alcohol drops substantially such that the hydroxyl proton can transfer to a proton accepting solvent molecule. 8-hydroxypyrene-1,3,6-trisulfonic acid sodium salt (HPTS, see Figure 1A) is a commonly used photoacid because of its high quantum yield and its small tendency to aggregate, a direct result of the −3 ground state charge.[2] In bulk water, the ground state of HPTS has a pK_a value of 7.8; however, in the first excited state, this value drops to 0.5. Therefore, the formation of the HPTS

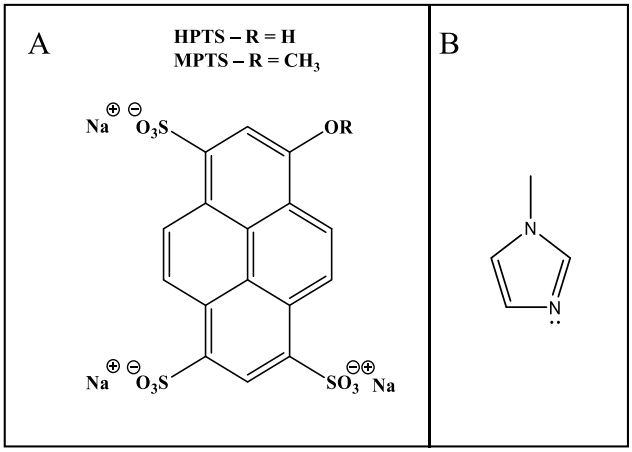

Figure 1. (A) Chemical structures of 8-hydroxypyrene-1,3,6-trisulfonic acid sodium salt (HPTS) and 8-methoxypyrene-1,3,6-trisulfonic acid sodium salt (MPTS). R = H for HPTS and R= CH_3 for MPTS. (B) The chemical structure of 1-methylimidazole.

Received: June 17, 2020
Revised: July 30, 2020
Published: August 10, 2020

https://dx.doi.org/10.1021/acs.jpcb.0c05525
J. Phys. Chem. B 2020, 124, 7897−7908

conjugate base in the excited state is highly favored in a proton accepting solvent.[14]

In water, the initial steps in the observed HPTS photodynamics occur on a very short time scale.[15,16] Following a dynamic Stokes shift on the hundreds of femtosecond time scale, the initial step in proton transfer (the formation of what is referred to as a contact ion pair) occurs on a few ps time scale.[15] In ∼90 ps, the proton becomes solvent separated.[15] On an even longer time scale, the proton (hydronium cation) can undergo longer-range proton transport because water is both a proton acceptor and donor. Some of these solvent separated protons will return to the deprotonated O^- of the HPTS and reform the contact ion pair, which is referred to as geminate recombination.[3,4,12,16] These various steps are tracked by spectral changes of HPTS using time-dependent fluorescence or transient absorption experiments.[13,17−20]

In the study presented here, we examine in detail the nature of proton transfer from HPTS to a proton acceptor, 1-methylimidazole (MeIm, Figure 1B). MeIm is an aprotic proton acceptor, and because it is aprotic, it is not a proton donor. Therefore, the contribution to the HPTS spectral dynamics from geminate recombination is eliminated. 1-methylimidazolium, the conjugate acid of MeIm, has a pK_a of ∼7, making MeIm a relatively good base.[21] Complete deprotonation of excited state HPTS is observed. The experiments and analysis presented below explicate the details of proton transfer in the aprotic pure liquid MeIm. The absence of significant recombination dynamics in HPTS/MeIm focuses our observations on the deprotonation mechanism of HPTS. This study aims to uncover the details of those deprotonation dynamics without considering complications added by recombination.

A recent paper by Kimura and co-workers studied the behavior of multiple photoacids in various protic room temperature ionic liquids.[22] The experiments found that in some cases a third spectral band was observed, in addition to the two spectral bands associated with the protonated and deprotonated photoacid species that are generally observed. This third peak was assigned as an associated state in which the photoacid and the acceptor solvent molecule share the proton to some extent. Previous studies by Inoue and co-workers have also suggested this behavior for the photoacid 9-hydroxyfluorenone in mixtures of toluene and 1-methylimidazole. In both of these studies, the third "associated" state was observed as a unique peak with an emission maximum between the protonated and deprotonated states.[23] This assignment is consistent with the idea that the fluorescence emission maximum is dependent on the amount of electron density in the photoacid π system.[24,25]

In the results presented below, the entire fluorescence spectral range of the emission of HPTS is recorded as a function of time over the full time window of the dynamics. The time-dependent fluorescence spectra are determined using time-correlated single photon counting measurements taken at a wide variety of wavelengths. The time-dependent fluorescence displays four distinct fluorescence bands that appear and decay on different time scales. We refer to these four time-dependent HPTS fluorescence bands as protonated (P), associated I (A_I), associated II (A_{II}), and deprotonated (D). Judging from the emission wavelengths, the associated species involve a slight sharing of the proton between the HPTS and the MeIm, but far from full proton transfer. The simple kinetic scheme of P → A_I → A_{II} → D does not describe the data well. A number of other kinetic pathways were tested. The best fit to the data has P going into A_I which mainly goes on to deprotonation (D), but A_I also feeds into A_{II}. A_{II} either returns to A_I or decays to the ground state and does not lead to deprotonation within experimental error. Quantum chemistry and first-principles molecular dynamics simulations provide evidence that A_I and A_{II} are two H-bonding configurations of MeIm to the HPTS hydroxyl, corresponding to axial and equatorial conformations.

2. MATERIALS AND METHODS

2.1. Experimental Methods. MeIm was purchased from Sigma-Aldrich, which was purified through distillation to have a purity ≥99%. Due to the incredibly hygroscopic nature of MeIm, the sample bottle was opened only in a glovebox to limit water content, which was verified to be ∼100 ppm through Karl Fischer titration. HPTS and MPTS were also purchased from Sigma-Aldrich and stored in a −20 °C freezer. Samples for the fluorescence experiments were prepared such that the final concentrations of the fluorescent probes in the MeIm were 10^{-4} M. Samples were injected into 1 mm path length cuvettes, which were stoppered and further sealed with parafilm to avoid water contamination. MeIm was found to have a negligible degree of background fluorescent emission from a small amount of an unknown fluorescent impurity. Due to high purity of the MeIm, the background fluorescence of the samples was determined to be orders of magnitude lower than that of the HPTS or MPTS probes, resulting in a negligible contribution to the emission signals rendering background subtraction unnecessary.

Population decays and orientational dynamics experiments were conducted utilizing time-correlated single photon counting (TCSPC). A Ti:sapphire oscillator producing ∼100 fs pulses at an excitation wavelength of 730 nm was employed. This wavelength was frequency doubled in a barium borate crystal to 365 nm for excitation of HPTS and MPTS samples. The bandwidth of the 365 nm excitation pulse was 5.8 nm. The laser repetition rate was lowered from 80 to 5 MHz by means of an acousto-optic single pulse selector. A computer-controlled half wave plate rotated the excitation beam such that measurements could be collected at magic angle relative to a fixed polarizer secured at the entrance slit of a monochromator. The sample was excited from the front surface in a near-normal geometry through a hole in the lens that collected the fluorescence. A second lens imaged the fluorescence onto the monochromator entrance slit. The fluorescence was frequency resolved by the monochromator, and single photons were detected with a multichannel plate (MCP) detector at wavelengths ranging from 400 to 600 nm in 2 nm increments. Each wavelength scan of the emission was collected for 15 s. The wavelength scan was repeated until it was determined that an acceptable signal-to-noise level had been reached. The data were taken such that all experimental parameters, including entrance and exit slit widths, were constant throughout the course of the experiment.

The instrument response was obtained by measuring the fluorescence emission of aqueous acidified malachite green with an optical density matching that of the sample, and under identical experimental conditions as the sample measurements. Malachite green has an extremely short fluorescence lifetime, 5 ps, which is short compared to the instrument response.[26] Measurement of its fluorescence emission gives the instrument response including the effects of the finite thickness of the

https://dx.doi.org/10.1021/acs.jpcb.0c05525
J. Phys. Chem. B 2020, 124, 7897−7908

sample cell. The instrument response was no greater than 70 ps.

2.2. Computational Methods. Our overall computational methodology involves multiple steps. First, we perform ground state classical molecular dynamics to get snapshots of equilibrated/solvated structures. Second, we extract snapshots to obtain combined quantum mechanics/molecular mechanics (QM/MM) single point energies to get absorption spectra and further perform QM/MM Born−Oppenheimer molecular dynamics (BOMD) to follow the excited state evolution over time. Finally, we perform quantum mechanical (QM) optimizations on microsolvated structures to find stationary points and the minimum energy paths connecting them.

Partial charges for the MeIm and HPTS molecules were obtained via RESP fitting.[27] Geometric parameters for the methylimidazole were obtained from the general Amber force field (GAFF).[28] The S−O parameters (bond, angle and torsion) for the sulfate group on the HPTS molecule were obtained from previous work,[29] with the remaining nonsulfate geometric parameters taken from GAFF.

One HPTS molecule was neutralized with 3 Na^+ ions and solvated with a box of 452 MeIm molecules. After an initial density and temperature equilibration to 300 K, production simulations were run in duplicate for 100 ns each using pmemd.cuda from AMBER14.[30,31] These were run with periodic boundary conditions and a 1 fs time step in the NPT ensemble, where T = 300 K and P = 1 atm. Temperature was maintained with a Langevin thermostat,[32] using a friction parameter δ = 5 ps^{-1}.

Snapshots from the ground state dynamics were selected via clustering analysis, as described in the Supporting Information (SI). Each structure was trimmed to a sphere of approximately ∼18 Å, retaining the closest 200 MeIm molecules to the center of the HPTS molecule. The QM region for subsequent QM/MM BOMD simulations was composed of HPTS, 3 Na^+ ions, and the 4 MeIm molecules that were closest to the hydroxyl oxygen on HPTS. Geometry optimizations and transition state calculations used this same QM region in vacuum.

Electronic structure calculations were performed using TeraChem[33,34] interfaced to OpenMM[35] for the MM region. Using the 6-31G** basis set and the ωPBE TDDFT functional with range separation parameter ω = 0.35 $bohr^{-1}$, the three lowest singlet excited states were computed with 6 initial guess vectors for the initial single point energies from classical trajectory structures. This value of ω was determined as the lowest value that ensured the absence of spurious low-lying charge transfer states involving the sodium ions.

Dynamics on S_1 was performed with QM/MM starting from nine snapshots obtained from the ground state MM dynamics. Each of these was run in the NVE ensemble for 1.5 ps using a 1 fs time step. For comparison, a further six snapshots were first minimized with QM/MM on S_0 and then promoted to S_1 and followed for 1.1 ps each. These were not significantly different from the snapshots that were run on S_1 without QM/MM optimization.

The QM region containing 1 HPTS, 3 Na+, and 4 MeIm molecules was extracted for further computations using ωPBE TDDFT (ω = 0.35, 6-31g**) in the gas phase. Transition states connecting optimized critical points were obtained with the nudged elastic band (NEB) method[36] using 17 beads and freezing the initial and final geometries.

3. RESULTS AND DISCUSSION

3.1. Experimental Results and Kinetic Model. The population decays of HPTS in MeIm were acquired from 400 to 600 nm in 2 nm increments resulting in 101 traces at distinct wavelengths. Figure 2 displays a few of the decays at several wavelengths. The data at the bluer wavelengths, such as 460 nm, decay very quickly whereas redder data, such as 510 nm, display a buildup. Note that the semilog plot emphasizes the depletion more than the buildup. At longer times, all of the curves decay as single exponentials with a decay time constant of 4.55 ns, the HPTS deprotonated state lifetime. It should be noted that regardless of emission wavelength, by ∼3 ns all traces decay with the same exponential decay time constant, indicating the absence of geminate recombination, which in water is manifested as a long time power law decay.[16] This is unsurprising given the documented basicity of MeIm. The ability of MeIm to serve as both an aprotic solvent as well as a Lewis base allows one to study the deprotonation dynamics of HPTS in great detail without added complexity from geminate recombination.

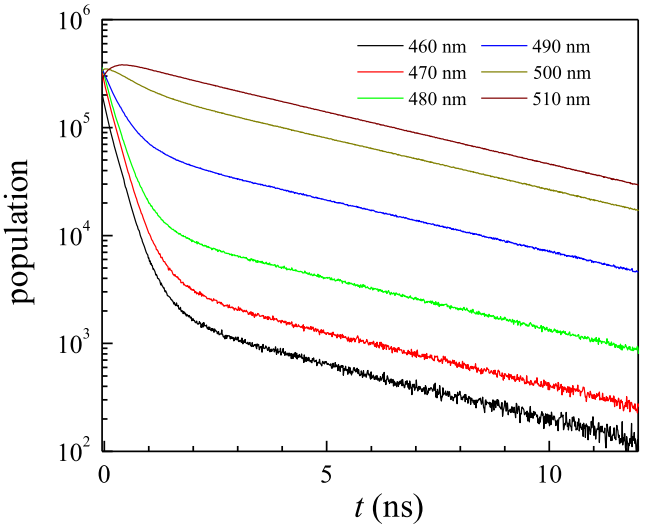

Figure 2. Population decay of HPTS in MeIm at a number of wavelengths. Shorter wavelength emissions undergo an initial rapid depletion as opposed to longer wavelength emissions that display a buildup. All wavelengths undergo single exponential decay after ∼3 ns.

As all of the population decays were collected under identical experimental conditions, time-dependent amplitude differences of various wavelength traces are the result of either photochemistry or of lifetime differences between multiple HPTS species. By plotting the relative amplitudes of each wavelength trace at a given time, the time-dependent emission peak shapes were reconstructed. This data analysis method is commonly used and has yielded excellent results in other fluorescence experiments, such as time-dependent Stokes shift measurements.[37,38] The emission peak shape undergoes dramatic changes with time. Since it is the emission line shape change that is the main interest of the data analysis, to directly compare different time slices minimizing the influence of population decay, each spectrum for a particular time was normalized such that the area under each trace is 1. This is a common practice in the analysis of photochemistry.[39−41] By utilization of area normalization, changes in the band shapes

https://dx.doi.org/10.1021/acs.jpcb.0c05525
J. Phys. Chem. B 2020, 124, 7897−7908

are highlighted. In the case of HPTS, the protonated species has been observed with an emission center near 440 nm, while the deprotonated peak is centered near 520 nm.[42]

The area normalized population of HPTS in MeIm over the first nanosecond is shown in Figure 3. As mentioned

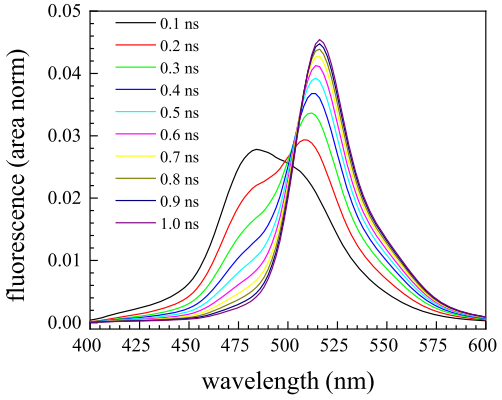

Figure 3. Area-normalized time-dependent fluorescence emission spectra of HTPS in MeIm. Population shifts are highlighted by utilizing this normalization method. Because the area under each trace has been normalized to 1, one can see the emission line shape changes without the effects of lifetime decay.

previously, the majority of the photochemistry occurs within 3 ns meaning the deprotonated peak can be cleanly isolated. At long time, the spectral band shape stops changing with time and simply decays with the fluorescence lifetime of the HPTS deprotonated state. By subtracting the long-time spectrum (taken at 15 ns) and renormalizing the data from Figure 3, a distinctly different third peak can be extracted from the data set, as shown in Figure 4A. As mentioned above, evidence of a third peak in photoacid studies has been seen in previous studies and has been attributed to a state in which the proton is shared by the photoacid and the Lewis base, in this case the MeIm molecule.[22,23] Given the basicity of MeIm, the presence of somewhat shared proton states is plausible as has been previously suggested.[22,23]

The protonated state of HPTS generally has a peak maximum of ~440 nm, and the deprotonated peak has a maximum of ~520 nm.[42] For HPTS in MeIm, the three separated peaks shown in Figure 4B have maxima at 480, 505, and 520 nm; none of these correspond to the wavelength that is commonly identified as the protonated state emission maximum. For this reason, experiments were conducted on MPTS. MPTS is a molecule similar to HPTS structurally, with a methoxy group replacing the photoacid hydroxyl (see Figure 1A). Because it cannot undergo deprotonation, it is a useful fluorophore as a control in HPTS experiments. The substitution of a methoxy group for an alcohol only has a minor impact on the fluorescence emission maximum. To verify the similarity, steady state fluorescence emission spectra of HPTS and MPTS were taken in 1-ethyl-3-methylimidazolium bis(trifluoromethylsulfonyl)imide (EmimNTf$_2$). The NTf$_2^-$ anion is a poor Lewis base despite its overall negative charge. Therefore, HPTS does not deprotonate upon excitation in EmimNTf$_2$. Figure 5 shows the steady state fluorescence emissions of HPTS and MPTS in EmimNTf$_2$, both excited at 365 nm to match time-dependent experimental conditions. From these spectra, it is clear that HPTS does not deprotonate. The emission maximum is very similar to that of

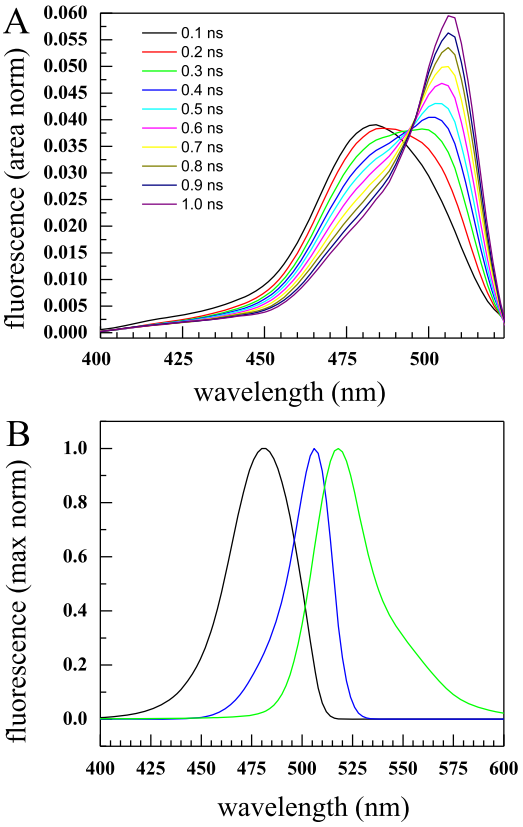

Figure 4. (A) Area-normalized time-dependent fluorescence emission spectra of HPTS in MeIm with long-time line shape (15 ns) subtracted. Upon subtraction of the long-time spectrum, it becomes evident that there are in fact multiple remaining peaks centered at 480 and 505 nm. The 505 nm peak was previously unseen due to high overlap with the other HPTS species. (B) Three fluorescence spectral can be cleanly separated to give the deprotonated HPTS peak as well as the two additional peaks that comprise the data in panel A.

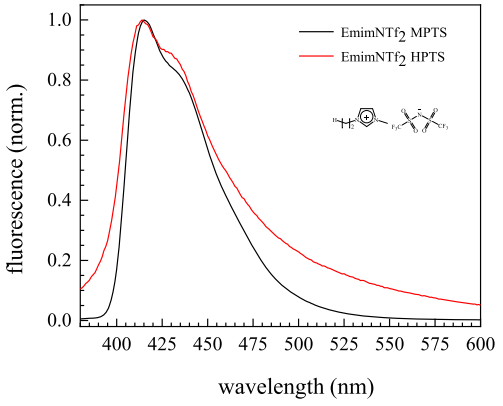

Figure 5. Steady state fluorescence emission spectra of HPTS and MPTS in the ionic liquid EmimNTf$_2$. The emission maxima are virtually the same in this solvent in which HPTS does not undergo proton transfer. Therefore, the emission maximum of MPTS is a good indicator of the frequency at which protonated HPTS should emit in a solvent in which it will undergo proton transfer.

MPTS. To help determine the origin of the HPTS band that peaks at ~480 nm (see Figure 4B), the absorption spectrum and steady state emission spectrum of MPTS in MeIm are shown in Figure 6A and compared in Figure 6B to the absorption spectrum of HPTS as well as the bluest peak (~480

https://dx.doi.org/10.1021/acs.jpcb.0c05525
J. Phys. Chem. B 2020, 124, 7897−7908

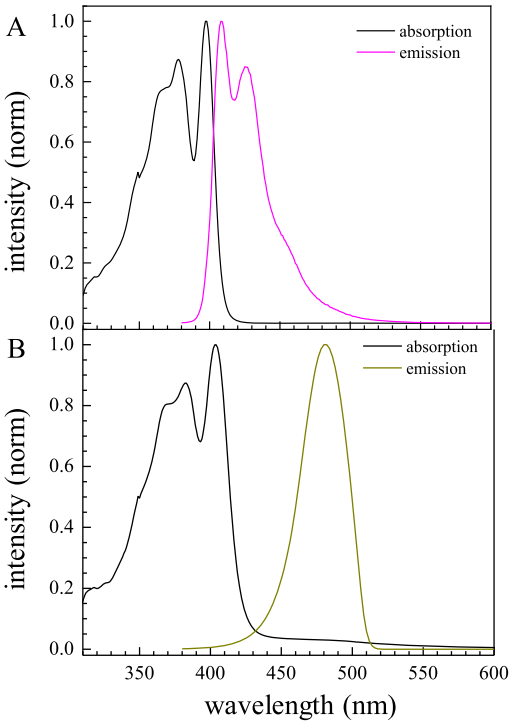

Figure 6. (A) UV−vis absorption and steady state fluorescence spectrum of MPTS in MeIm solution. (B) UV−vis absorption and the 470 nm emission of HPTS in MeIm solution. The shift in the HPTS emission indicates that this is not emission from protonated HPTS.

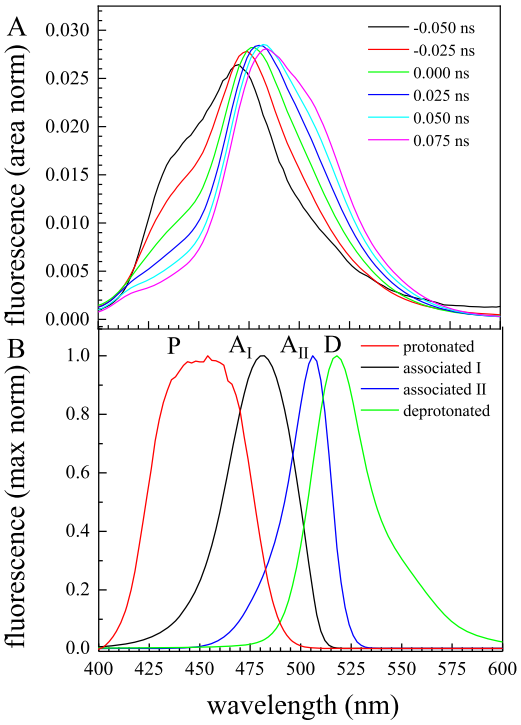

Figure 7. (A) Area-normalized fluorescence emission spectra of HPTS in MeIm at various times immediately before and after the time $t = 0$. These data clearly show the existence of a fourth state of HPTS which decays within the time scale of the instrument response. The short time fluorescence spectrum is from protonated HTPS. (B) All four fluorescence bands obtained from the time-dependent data. From high frequency to low, they are protonated HTPS, associated I, associated II, and deprotonated HPTS.

nm) isolated in the time-dependent data. This is highly suggestive that the observed 480 nm peak is not the protonated HPTS peak. The possibility that the HPTS molecule begins in a proton-shared state is also unlikely because the absorption spectra of MPTS and the HPTS are very similar.

In most TCSPC measurements, time $t = 0$ is assigned to the maximum of the instrument response function without issue. However, it is possible to find situations in which important dynamics occur within the instrument response. The disparity between the expected peak emission of the HPTS protonated peak and the observed 480 nm peak indicates the presence of yet another peak. Figure 7A displays a plot of area normalized data over the time range of the instrument response. There is clear evidence of a fourth population bluer than 480 nm.

As discussed below, the short-time component has a decay time of ∼30 ps. It is possible to extract the emission line shape of the short time component of HPTS by taking the line shape of the previously identified peak centered ∼480 nm (seen in Figure 4B) and performing a scaled subtraction of it from the spectrum at −0.05 ns. The convolve-and-compare fitting method to obtain the time-dependence, which aids in determining the spectrum, is presented below.

Figure 7B shows a plot of all four time-dependent spectra. We assign these peaks as a protonated species (P), two associated species in which the proton is partially shared between the HPTS and MeIm (A_I and A_{II}), and the deprotonated species (D). The low signal at the rising edge of the instrument response makes the protonated HPTS spectrum lower quality than the other extracted peaks. Looking at the steady state emission spectrum of MPTS in Figure 6A, it can be seen that there is a large vibronic band to the red of the emission origin. The HPTS P spectrum is composed of these two bands that are unresolved.

To obtain the very short time behavior, it is necessary to separate the relative contributions of the spectral dynamics from the instrument response. This is done using the convolve-and-compare method. The instrument response can be modeled as a Gaussian, and the populations can be fit as a series of exponentials. σ is the standard deviation of the Gaussian instrument response (30 ps) of the TCSPC instrument. Normally when convolution is performed, the population decays are fit to a sum of decaying exponentials.[43−45] However, in this case the protonated state feeds into the associated states, which makes it necessary to include growing terms in addition to decaying terms to represent the contribution to the signal from each of the different populations. Equation 1 is the convolution.

$$P(t) = (A - Be^{-t/\tau_{prot}})e^{-t/\tau_{assoc}} * Ce^{-t^2/2\sigma^2} \quad (1)$$

$P(t)$ is the observed population at short time including convolution with the instrument response. The "*" indicates convolution. A and B both are amplitudes, and τ_{prot} and τ_{assoc} are the protonated and the A_I associated time constants. As discussed below, τ_{assoc} was fixed to 0.23 ns to match the rate at which the final full deprotonation of the A_I state is observed.

Equation 1 was used to fit a subset of wavelengths where the protonated species could be observed. τ_{prot} was obtained by simultaneously fitting multiple wavelengths. In addition to fixing τ_{assoc}, τ_{prot} was a shared parameter while the amplitude terms were free parameters. The fits to the rising edge of the

https://dx.doi.org/10.1021/acs.jpcb.0c05525
J. Phys. Chem. B 2020, 124, 7897−7908

data are shown in Figure 8. The fits are high quality. The decay time of the protonated state was determined to be 30 ± 15 ps.

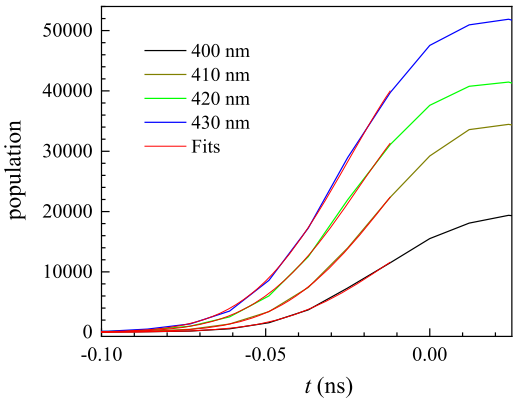

Figure 8. Short time fluorescence data and several fits that include convolution with the instrument response function. The fits yield a 30 ± 15 ps depletion time of the protonated state.

While the error bars are large because of the convolve-and-compare procedure, the results show that the initial partial deprotonation to the associated states occurs very rapidly, much faster than the decays of the other species (see below). Therefore, the uncertainty in the decay of P does not affect the determination of the kinetics of the overall process.

With the identification of the P spectrum and its decay constant, we want to understand the global dynamics of the four state system using a kinetic model. Between the four states, transfer time constants, and excited state lifetime decays, the number of adjustable parameters is quite large, so it is important to identify some of the terms. By integrating the fluorescence emission over all wavelengths at each collected time point, the total HPTS population decay can be extracted regardless of which state the HPTS molecule is in at any given time. Figure 9 shows the total population decay. This data fit

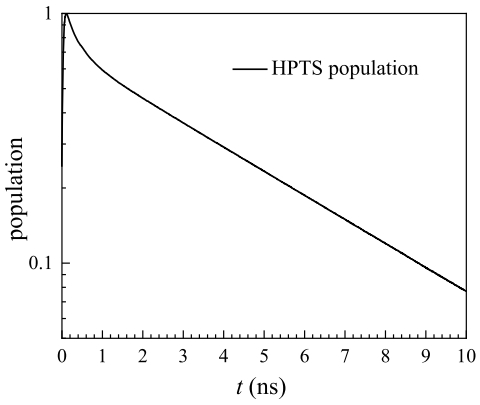

Figure 9. Semilog plot of the total HPTS population decay obtained by integrating the emission spectrum over wavelength at each time. The data is not a single exponential.

to a biexponential with a fast component of 0.35 ns and a slow component 4.55 ns. The 4.55 ns decay is the decay to the ground state of the deprotonated HPTS. This decay matches the long-time decays shown in Figure 2. At long time, only the deprotonated spectral band remains. The simplest explanation for the observed data (Figure 9) is that one or both of the associated states have a short lifetime. Previous studies of HPTS in AOT reverse micelles have observed subpopulations of HPTS with short lifetimes, showing that the lifetime can be strongly affected by the solvent environment.[42] By having these decay time constants, it is possible to fix a number of the adjustable parameters. Kinetic models were further simplified by assuming that a negligible number of molecules in the A_I state are lost by decay to the ground state. This assumption is supported by the fact that the overwhelming majority of the A_I state has decayed before the first nanosecond. As shown below, the vast majority of A_I rapidly decays to the deprotonated state, D.

Following the 30 ps decay of the protonated state, one can fit the time-dependent fluorescence emission data as a linear combination of the three peaks shown in Figure 4b to extract the relative populations of each distinct HPTS state as a function of time. The simplest model has each state feeding directly into the next state (P → A_I → A_{II} → D), going from the bluest peak to the reddest peak until only the final deprotonated peak is left, which decays according to its 4.55 ns lifetime. That is, the protonated state feeds into the A_I state, which feeds into the A_{II} state, which feeds into the deprotonated state. This scheme is shown in the top of Figure 10A. The data and the fits to the data using this "direct" model are shown in Figure 10A. It is immediately clear that the quality of the fits using the direct model is quite poor. The main difficulty with this model is that there is far less amplitude passing through the A_{II} band than enters the deprotonated band. This causes the model to fail in multiple ways. The A_{II} state is forced to decay far too quickly and the deprotonated

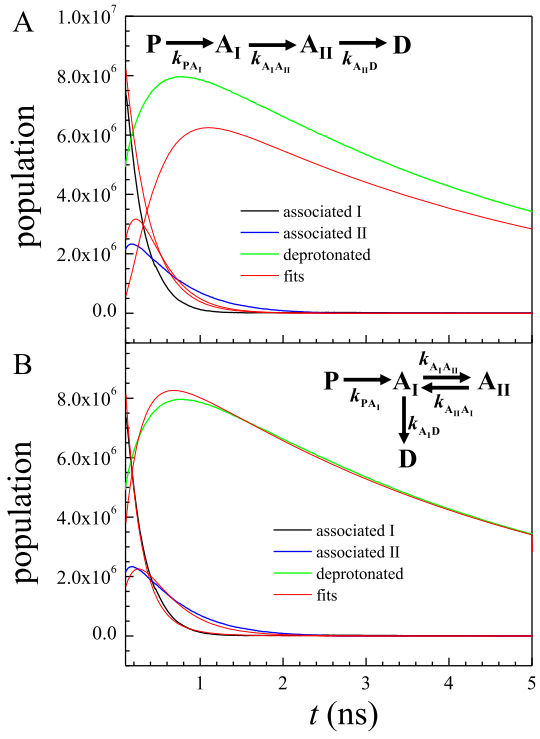

Figure 10. Time-dependent emission data for the associated I, associated II, and deprotonated bands. (A) The sequential model, shown in the inset, in which each state feeds into the next state. The simultaneous fit to this kinetic model is poor. (B) The kinetic model in which the population transfer is branched. The fit is very good. The dominant pathway is P to A_I to D. Deprotonation does not occur from the A_{II} state.

https://dx.doi.org/10.1021/acs.jpcb.0c05525
J. Phys. Chem. B 2020, 124, 7897−7908

state is both rising too slowly and never coming close to the experimental amplitude before it begins to decay with the lifetime. One can fix the rate constant in the rate equation for $A_I \rightarrow A_{II}$, $k_{A_IA_{II}}$, (see inset Figure 10A) to fit the associated I band (A_I) well. However, doing this make the overall fits to the data much worse than the fit shown in Figure 10A. These results show that the sequential direct kinetic model is not correct.

A large number of kinetic models were tried. It was found that any model that has significant deprotonation coming from A_{II} ($A_{II} \rightarrow D$) produced fits akin to those shown in Figure 10A. The inset in Figure 10B shows the model that works well and is additionally supported by quantum chemistry and dynamics simulations that also identify the A_I and A_{II} states, as detailed in the following.

3.2. Computational Matching of Emission Spectra. We started with 100 ns of classical molecular dynamics on the ground state for a system of one HPTS molecule, 3 Na^+ ions, and 452 MeIm molecules to investigate potential initial solvated states of the HPTS. The HPTS molecule adopted two conformations over the course of the dynamics, related by twisting around the C−C−O−H dihedral angle. We define these conformations as axial (O−H bond is approximately parallel to the long axis of HPTS) and equatorial (O−H points is approximately parallel to the short axis of HPTS), depicted schematically in Figure 11. The equatorial conformation was substantially less common than the axial, with flips occurring once every 50 ns on average (Figure S1). Representative structures for these two geometries are depicted in Figure 12C,D. In both cases, a single MeIm molecule is hydrogen-bonded to the hydroxyl group. This hydrogen bond is maintained when flipping from axial to equatorial. Solvent exchange, where the identity of the hydrogen-bonding MeIm molecule switches, was observed approximately every 10 ns (Figure S2). Given the rarity of the equatorial conformation, the dominant species on the ground state is clearly the axial conformation, as confirmed by clustering analysis (Figure S3). However, we note that the absorption spectra for axial and equatorial conformations are predicted to be quite similar (Figure S4). Thus, the computations do not exclude the possibility that there might be some minority contribution from the excitation of conformations that are equatorial on S_0. The predicted absorption maximum (3.9 eV, Figure S4) is blue-shifted from the experimental absorption spectrum (3.1 eV, Figure 6). Such blue shifts are often observed when including significant amounts of exact exchange in the exchange-correlation functional (here indicated by the large value of the range-separation parameter ω). It is necessary to include significant amounts of exchange to avoid spurious low-lying charge-transfer states that would otherwise occur in TDDFT (especially in the present case, due to the high charge on HPTS and the presence of three Na^+ cations).[46]

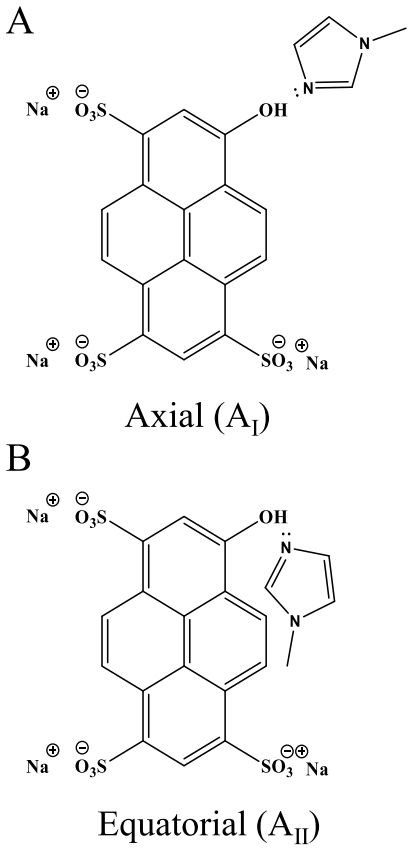

Figure 11. Schematic illustrations of the hydrogen bonding structures for the two states (A) axial, associated I (A_I), and (B) equatorial, associated II (A_{II}).

A set of nine snapshots was taken from the ground state MM dynamics to initiate QM/MM BOMD on the S_1 excited state for 1.5 ps each. The snapshots were chosen to include equatorial and axial conformations, in addition to sampling hydrogen bond distances and alternative solvent organization in the first solvation shell (as determined by clustering analysis, detailed in Figure S3). A representative depiction of the full QM/MM system is given in Figure 12A, with the relevant QM region shown in Figure 12B. All of the snapshots taken directly from the classical MD sampling had a similar excitation energy/oscillator strength with little to no differentiation on the basis of hydrogen bond distance, solvent configuration, or geometry of HPTS (see Figure S3). However, after 1.5 ps of QM/MM-AIMD on S_1, the computed emission wavelengths diverge between trajectories corresponding to initial axial and equatorial conformations. In Figure 12C,D, we compare histograms of the emission wavelengths for trajectories started in axial (Figure 12C) and equatorial (Figure 12D) conformations, separating the first and last 500 fs of the 1.5 ps time evolution. The time-resolved fluorescence barely changes for the axial conformations but exhibits a noticeable spectral shift for the equatorial conformations. This led us to suspect that transitions between axial and equatorial conformations might occur on S_1 and this could contribute to the observed distinct time-resolved emission spectra.

To investigate the different species that might be involved in the excited state dynamics, we turned to the optimization of microsolvated clusters, choosing the same QM region used in the QM/MM dynamics (with four MeIm solvent molecules surrounding the HPTS chromophore). We located S_1 minima for the axial and equatorial species (commencing the optimizations from initial geometries extracted from the QM/MM dynamics simulations). In agreement with previous work on HPTS in aqueous solution,[47,48] we find evidence that hydrogen bonding is strengthened on S_1 based on the decrease in N−H bond distance. Both the axial and equatorial conformations exhibit increased proton sharing, as judged by the O−H and N−H bond distances. Key geometric parameters for the axial and equatorial minima on S_0 and S_1 are provided in Figure S12. In addition to the strengthened hydrogen

https://dx.doi.org/10.1021/acs.jpcb.0c05525
J. Phys. Chem. B 2020, 124, 7897−7908

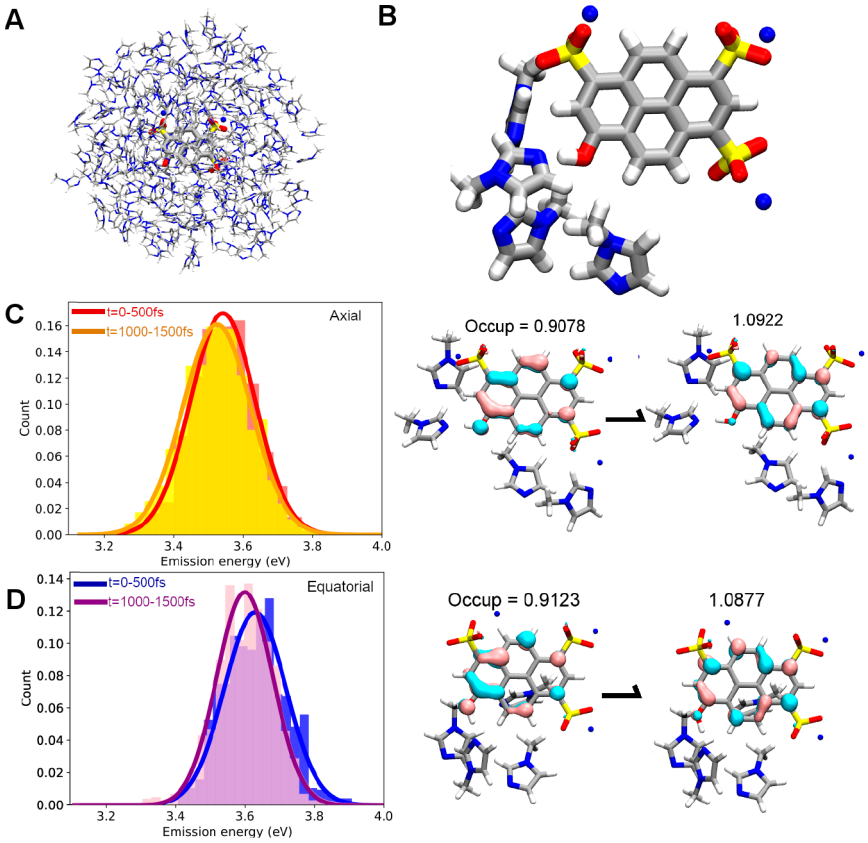

Figure 12. Full QM/MM system used in excited state dynamics is shown in panel A, with the QM region shown in panel B. Overlaid histograms of the emission energies over the course of the dynamics for axial (panel C) and equatorial (panel D) conformations are shown in 500 fs intervals, along with the excited state natural orbitals for the first excited state transition at the computed S_1 minimum, with occupation numbers shown for each.

bonding on S_1, we noted that the axial and equatorial S_1 minima have distinct predicted fluorescence maxima. Compared to the initial vertical excitation energy at the S_0 axial minimum, the axial conformation is red-shifted by 0.41 eV and the equatorial conformation is red-shifted by 0.60 eV. These shifts are in good agreement with the observed red-shifts (from the experimental absorption maximum) for the A_I and A_{II} fluorescence spectra (0.52 and 0.65 eV, respectively). Thus, we identify the A_I and A_{II} species as axial and equatorial conformations on S_1.

3.3. Deprotonation Pathways. We also searched for deprotonated S_1 minima of the microsolvated cluster, starting from both axial and equatorial conformations. Despite considerable effort, we were unable to locate an equatorial deprotonated conformation (constrained minima all return to either an equatorial protonated conformation or an axial conformation upon unconstrained optimization). We did locate an axial deprotonated conformation (Figure S13), and we find that its emission energy is red-shifted by 0.64 eV relative to the axial absorption energy. This can be compared with a measured red-shift of 0.71 eV for the emission energy of the deprotonated band ("D" in the discussion above).

The kinetic model suggested by the calculations can be inferred from Figure 13 and is largely in agreement with the deductions made above from model fitting of the experimental data. On the ground state, the HPTS molecule is primarily found hydrogen-bonded in the axial conformation (S_0 Min on the left side of the dotted line in Figure 13). After photoexcitation, the molecule can relax to the A_I emissive state, which is an S_1 minimum in the axial conformation. As detailed in Figure S11, there is increased proton sharing in this geometry, consistent with a strengthening of the HPTS/MeIm hydrogen bond. From the A_I state, the molecule can either transition to the A_{II} state (an S_1 minimum with hydrogen bonding in the equatorial conformation) or it can proceed to deprotonation (the D state).

Using nudged elastic band (NEB),[36] we optimized minimal energy pathways for $A_I \rightarrow A_{II}$ and $A_I \rightarrow D$ reactions on S_1. As shown in Figure 13, the barriers along these pathways are similar, with a slight preference for the A_I to A_{II} pathway. The "productive" deprotonation pathway $A_I \rightarrow D$ and the "non-productive" isomerization pathway $A_I \rightarrow A_{II}$ are highlighted with dotted red lines on Figure 13, and the energy of the transition state for each reaction (structures available in Figure S12) is depicted (labeled "TS"). The computed barriers from NEB are 30 and 26.5 kcal/mol for the $A_I \rightarrow D$ and $A_I \rightarrow A_{II}$ pathways, respectively. The absolute values of these barriers would likely decrease with a more complete description of the solvent environment, which might switch the ordering to be consistent with the experimental finding that $A_I \rightarrow D$ is faster than $A_I \rightarrow A_{II}$.

Additionally, we have optimized the reaction path for $A_I \rightarrow A_{II}$ on S_0. The resulting barrier is higher (29 kcal/mol) than the 26.5 kcal/mol barrier on S_1, indicating that the axial to equatorial transition is significantly more likely to occur on S_1 than it is on S_0. In agreement with this, the kinetic modeling based on the experimental data did not find any need for

https://dx.doi.org/10.1021/acs.jpcb.0c05525
J. Phys. Chem. B 2020, 124, 7897−7908

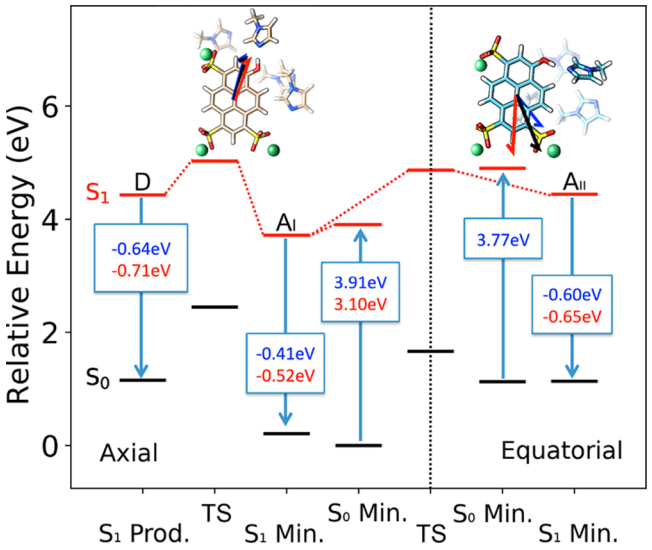

Figure 13. Relative energies for various minimized (in vacuum) QM critical points for both axial (left) and equatorial (right) conformations, with the S_0/S_1 energies shown in black/red. The relevant dipole moments are shown on the representative geometries in red (S_1) and black (S_0), with the transition dipole moment shown in blue. Computed vertical excitation energies (blue) and measured absorption maxima (red) are shown for the axial and equatorial Franck–Condon points (experimental absorption maximum for equatorial conformation is not available). Computed (blue) and measured (red) emission energies are shown at S_1 minima, depicted as shifts from the axial absorption maximum. Red dotted lines connect the predicted kinetic pathways for axial ($P \rightarrow A_I \rightarrow TS \rightarrow D$) and equatorial ($A_I \rightarrow TS \rightarrow A_{II} \rightarrow TS \rightarrow A_I$).

consideration of direct population of A_{II} during photoexcitation.

As discussed above, we cannot locate a deprotonated S_1 minimum for the equatorial conformation. However, the A_{II} species could decay through nonradiative pathways in addition to radiative fluorescence. Because we are using TDDFT, which is not able to describe S_0/S_1 conical intersections,[49] we could not elucidate the nature of potential nonradiative pathways in this work. This could be explored in the future using multireference methods that are able to describe S_0/S_1 intersections.

The distinction between the P and A_I states remains incompletely characterized by the computational modeling. The transition from P to A_I could correspond to cooperative solvent rearrangement after photoexcitation that cannot be described with the microsolvated cluster (containing only four MeIm solvent molecules) and also takes longer than the 1.5 ps time scale accessible to the excited state QM/MM simulations. The time scale for depletion of P is in line with expected solvent reorganization times (few tens of ps), as judged by solvation dynamics studies. Larger scale and/or longer time excited state QM/MM dynamics simulations could be used in the future to shed further light on the nature of the P state and the solvent relaxation that gives rise to it.

3.4. Finalized Kinetic Model and Connections between Experiment and Theory. In the kinetic model, the path to deprotonation is P to A_I to D. The decay of A_I and the growth and decay of D are captured quite well. The relatively small population in A_{II} flows in from A_I. The growth and rapid decay of A_{II} are also captured reasonably well by fitting with the kinetic equations that arise from the scheme shown in the inset in Figure 10B. Adding a path from A_{II} to D does not change the fit, which means that either zero or negligible deprotonation occurs from the A_{II} state. This is consistent with our inability to find a deprotonated equatorial conformation in the simulations. In the inset shown in Figure 10B, population flowing from A_I to A_{II} can return to A_I. The A_{II} population is small even at its maximum at ~170 ps. Because its population is always very small, the model cannot distinguish between A_{II} losing some population back to A_I or only decaying with a fast time constant to the ground state. The results show that the kinetics of deprotonation occur almost exclusively via the $P \rightarrow A_I \rightarrow D$ pathway. The population and depopulation of A_{II} is a side process that has only a small effect on deprotonation but is important to understand the events that lead to the rise and fall of the four spectral peaks shown in Figure 7B. The rate constants obtained from fitting the kinetic equations that produced the fits in Figure 10B are as follows. $k_{A_IA_{II}} = 1.7\ ns^{-1}$; $k_{A_{II}A_I} = 0.49\ ns^{-1}$; $k_{A_ID} = 3.41\ ns^{-1}$; A_{II} lifetime = $2.5\ ns^{-1}$ (0.4 ns); D lifetime = $0.22\ ns^{-1}$ (4.55 ns).

The states A_I and A_{II} have been referred to as associated, with the proton to some extent having moved part way between its initial configuration as a hydroxyl and its final form as a hydrogen on the methylimidazolium cation. A_I and A_{II} are distinct species as shown by their spectra (see Figures 4 and 7B). Although the experiments and the data analysis show that A_I and A_{II} are intermediates between the protonated state and the deprotonated state, these are insufficient to determine the chemical nature of A_I and A_{II}. Thus, we turned to simulations, which show that A_I and A_{II} correspond to two distinct (axial and equatorial, respectively) H-bonding structures between HPTS and MeIm.

The difference between the two structures is the conformation of the MeIm molecule: axially hydrogen bonding to the HPTS (A_I) or equatorially hydrogen bonding to the HPTS (A_{II}). The simulations show that the A_I state is characterized by a small movement of the proton toward the MeIm (corresponding to increased proton sharing and hydrogen-bond strengthening). Although the distinction between P and A_I is not completely characterized by the simulations, we believe that the $P \rightarrow A_I$ transition is likely to be dominated by relaxation of the surrounding solvent. The simulations show that the equatorial conformer is negligibly populated on S_0. Hence, the A_{II} state is not generated by excitation of an equatorial conformer. Instead, the barrier to reorientation of the MeIm is lowered on S_1 (compared to S_0) and the A_{II} state has some probability of forming from A_I. The A_I to A_{II} pathway is a structural change in which the axial conformation transforms into the equatorial conformation. We speculate that the very short lifetime of A_{II} arises because of a nearby conical intersection. The simulations also suggest that the equatorial conformation does not proceed to full deprotonation of HPTS within the time scale suggested by the kinetic model. A similar observation was made by Tuckerman and co-workers in simulations studying imidazole phosphoric acid mixtures involving two imidazole molecules.[50] It should be noted that the simulations in that study observed picosecond time scales, while the findings presented in this work observe these stable conformers existing well into the nanosecond time regime. The axial and equatorial conformations have a small Zundel-like character, but the axial state can go on to complete deprotonation while the equatorial state

https://dx.doi.org/10.1021/acs.jpcb.0c05525
J. Phys. Chem. B 2020, 124, 7897–7908

remains in a Zundel-like structure and rapidly decays to the ground state.

4. CONCLUDING REMARKS

We have presented a detailed study of proton transfer from the photoacid HPTS to the proton acceptor 1-methylimidazole. Time-correlated single photon counting was used to reconstruct time-dependent spectra over the entire spectral range of the HPTS fluorescence from tens of picoseconds to >10 ns. Four spectral bands were observed with distinct time dependences (see Figure 7B). Immediately following excitation, the fluorescence band from the protonated state of HPTS was observed. This band is the highest frequency and is short-lived (30 ps). The protonated state decays into a state we have called A_I. A_I mainly decays into the fully deprotonated state, D, in which a proton has been transferred from HPTS to 1-methylimidazole to from the cation 1-methylimidazolium. This process occurs with a time constant (inverse of the rate constant) of ∼300 ps. The deprotonated state D decays to the ground state with a fluorescence lifetime of 4.55 ns. Because MeIm is a proton acceptor but not a proton donor, the kinetics are not complicated by additional solvent to solvent proton transfer and geminate recombination with the deprotonated HPTS. The A_I state also transfers a portion of its population to a second intermediate state, A_{II}, with an inverse rate constant of ∼600 ps. A_{II} does not go on to complete deprotonation. It can return some of its population to A_I (see inset in Figure 10B). It mainly decays to the ground state with a lifetime of 0.4 ns. By ∼2 ns, all of the HPTS molecules remaining in the excited state are in the deprotonated form (see Figure 10B).

Excited state QM/MM molecular dynamics simulations determined the nature of the A_I and A_{II} species (shown schematically in Figure 11 and with energetic details in Figure 13). These two species differ by the hydrogen bonding configuration of the MeIm to the HPTS. A_I has an axial hydrogen bonding configuration between the HPTS hydroxyl and the MeIm nitrogen lone pair, while A_{II} has equatorial H-bonding. The simulations show that the axial conformation dominates on the ground state. However, interconversion from the axial to the equatorial conformations becomes more facile in the excited state. The transfer of fluorescence intensity from the A_I band to the A_{II} band is caused by the conversion of the axial H-bond complex to the equatorial complex. The data and fits to the kinetic eqs (Figure 10B) are consistent with the equatorial complex not undergoing complete deprotonation, in agreement with the apparent lack of a deprotonated equatorial minimum on S_1 in the simulations. In contrast, the simulations located an axial deprotonated complex, suggesting proton transfer from the axial state that is consistent with the experiments and the data analysis. Intermediate states like A_I are commonly described as having the proton shared between the photoacid donor and the solvent acceptor in a Zundel-like state. The simulations indicate that there is movement of the proton away from the HPTS oxygen toward the MeIm nitrogen, but the shift in position is very small. So the associated states are not Zundel with essentially equal sharing of the proton between the donor and the acceptor.

This study provides insights into proton transfer in a nonaqueous solvent. Nonaqueous proton transfer is found in many chemical systems. MeIm is a proton acceptor but not a donor, which simplified understanding the observed dynamics in the HPTS/MeIm system. Similar molecules that are both proton donors and acceptor, e.g., imidazole and triazole, can undergo long-range proton transfer and may be useful in devices such as nonaqueous proton transfer membranes for high temperature fuel cells. As seen here, the structure of the proton transfer solvent and its conformation relative to a proton transfer partner can play an important role in the proton transfer dynamics.

■ ASSOCIATED CONTENT

Supporting Information

The Supporting Information is available free of charge at https://pubs.acs.org/doi/10.1021/acs.jpcb.0c05525.

Detailed results from classical molecular dynamics, clustering analyses, excited state dynamics calculations with alternative initial conditions, and geometric analyses and energetics of optimized microsolvated geometries; Cartesian coordinates for structures from QM/MM dynamics and geometry optimizations (PDF)

■ AUTHOR INFORMATION

Corresponding Author

Michael D. Fayer − *Department of Chemistry, Stanford University, Stanford, California 94305, United States; SLAC National Accelerator Laboratory, Menlo Park, California 94025, United States;* orcid.org/0000-0002-0021-1815; Phone: 650 723-4446; Email: fayer@stanford.edu

Authors

Joseph E. Thomaz − *Department of Chemistry, Stanford University, Stanford, California 94305, United States*

Alice R. Walker − *Department of Chemistry, Stanford University, Stanford, California 94305, United States; SLAC National Accelerator Laboratory, Menlo Park, California 94025, United States;* orcid.org/0000-0002-8617-3425

Stephen J. Van Wyck − *Department of Chemistry, Stanford University, Stanford, California 94305, United States*

Jan Meisner − *Department of Chemistry, Stanford University, Stanford, California 94305, United States; SLAC National Accelerator Laboratory, Menlo Park, California 94025, United States;* orcid.org/0000-0002-1301-2612

Todd J. Martinez − *Department of Chemistry, Stanford University, Stanford, California 94305, United States; SLAC National Accelerator Laboratory, Menlo Park, California 94025, United States;* orcid.org/0000-0002-4798-8947

Complete contact information is available at: https://pubs.acs.org/10.1021/acs.jpcb.0c05525

Author Contributions

§J.E.T. and A.R.W. contributed equally to this work.

Notes

The authors declare no competing financial interest.

■ ACKNOWLEDGMENTS

This work was funded by the Division of Chemical Sciences, Geosciences, and Biosciences, Office of Basic Energy Sciences of the U.S. Department of Energy Grant No. DE-FG03-84ER13251 (J.E.T., S.J.V.W., and M.D.F.). This material is based upon work supported by the U.S. Department of Energy, Office of Science, Office of Advanced Scientific Computing Research, Scientific Discovery through Advanced Computing (SciDAC) (T.J.M.). J.E.T. and S.J.V.W. thank the NSF for graduate research fellowships. J.M. thanks the German Research Foundation (DFG) for funding. We would also like

to thank P. L. Kramer, S. A. Yamada, and D. J. Hoffman for insightful discussions.

REFERENCES

(1) Springer, T. E.; Zawodzinski, T.; Gottesfeld, S. Polymer Electrolyte Fuel Cell Model. *J. Electrochem. Soc.* **1991**, *138* (8), 2334−2342.
(2) Hauser, M.; Haar, H. P.; Klein, U. Indirect Demonstration of the Coulomb Cage for Prototropic Dissociation. *Ber. Buns. Phys. Chem.* **1977**, *81* (1), 27−30.
(3) Agmon, N. Elementary Steps in Excited-State Proton Transfer. *J. Phys. Chem. A* **2005**, *109*, 13−35.
(4) Simkovitch, R.; Pines, D.; Agmon, N.; Pines, E.; Huppert, D. Reversible Excited-State Proton Geminate Recombination: Revisited. *J. Phys. Chem. B* **2016**, *120* (49), 12615−12632.
(5) Rini, M.; Magnes, B.-Z.; Pines, E.; Nibbering, E. T. Real-Time Observation of Bimodal Proton Transfer in Acid-Base Pairs in Water. *Science* **2003**, *301* (5631), 349−352.
(6) Mohammed, O. F.; Dreyer, J.; Magnes, B. Z.; Pines, E.; Nibbering, E. T. Solvent-Dependent Photoacidity State of Pyranine Monitored by Transient Mid-Infrared Spectroscopy. *ChemPhysChem* **2005**, *6* (4), 625−636.
(7) Mohammed, O. F.; Pines, D.; Dreyer, J.; Pines, E.; Nibbering, E. T. Sequential Proton Transfer Through Water Bridges in Acid-Base Reactions. *Science* **2005**, *310* (5745), 83−86.
(8) Knight, C.; Voth, G. A. The Curious Case of the Hydrated Proton. *Acc. Chem. Res.* **2012**, *45* (1), 101−109.
(9) Agmon, N. The Grotthuss Mechanism. *Chem. Phys. Lett.* **1995**, *244* (5), 456−462.
(10) Spry, D. B.; Goun, A.; Glusac, K.; Moilanen, D. E.; Fayer, M. D. Proton Transport and the Water Environment in Nafion Fuel Cell Membranes and AOT Reverse Micelles. *J. Am. Chem. Soc.* **2007**, *129* (26), 8122−8130.
(11) Geng, J.; Kim, K.; Zhang, J.; Escalada, A.; Tunuguntla, R.; Comolli, L. R.; Allen, F. I.; Shnyrova, A. V.; Cho, K. R.; Munoz, D.; Wang, Y. M.; Grigoropoulos, C. P.; Ajo-Franklin, C. M.; Frolov, V. A.; Noy, A. Stochastic Transport Through Carbon Nanotubes in Lipid Bilayers and Live Cell Membranes. *Nature* **2014**, *514* (7524), 612.
(12) Pines, E.; Huppert, D. Geminate Recombination Proton-Transfer Reactions. *Chem. Phys. Lett.* **1986**, *126* (1), 88−91.
(13) Sedgwick, M.; Cole, R. L.; Rithner, C. D.; Crans, D. C.; Levinger, N. E. Correlating Proton Transfer Dynamics to Probe Location in Confined Environments. *J. Am. Chem. Soc.* **2012**, *134* (29), 11904−11907.
(14) Leiderman, P.; Genosar, L.; Huppert, D. Excited-State Proton Transfer: Indication of Three Steps in the Dissociation and Recombination Process. *J. Phys. Chem. A* **2005**, *109* (27), 5965−5977.
(15) Spry, D. B.; Goun, A.; Fayer, M. D. Deprotonation Dynamics and Stokes Shift of Pyranine. *J. Phys. Chem. A* **2007**, *111*, 230−237.
(16) Agmon, N. Geminate Recombination in Proton Transfer Reactions. III. Kinetics and Equilibrium Inside a Finite Sphere. *J. Chem. Phys.* **1988**, *88*, 5639−5642.
(17) Rini, M.; Pines, D.; Magnes, B.-Z.; Pines, E.; Nibbering, E. T. Bimodal Proton Transfer in Acid-Base Reactions in Water. *J. Chem. Phys.* **2004**, *121* (19), 9593−9610.
(18) Spry, D.; Goun, A.; Glusac, K.; Moilanen, D. E.; Fayer, M. Proton Transport and the Water Environment in Nafion Fuel Cell Membranes and AOT Reverse Micelles. *J. Am. Chem. Soc.* **2007**, *129* (26), 8122−8130.
(19) Tunuguntla, R. H.; Allen, F. I.; Kim, K.; Belliveau, A.; Noy, A. Ultrafast Proton Transport in Sub-1-nm Diameter Carbon Nanotube Porins. *Nat. Nanotechnol.* **2016**, *11* (7), 639.
(20) Thomaz, J. E.; Lawler, C. M.; Fayer, M. D. Proton Transfer in Perfluorosulfonic Acid Fuel Cell Membranes with Differing Pendant Chains and Equivalent Weights. *J. Phys. Chem. B* **2017**, *121* (17), 4544−4553.
(21) Tu, C.; Silverman, D. N.; Forsman, C.; Jonsson, B. H.; Lindskog, S. Role of Histidine 64 in the Catalytic Mechanism of Human Carbonic Anhydrase II Studied with a Site-Specific Mutant. *Biochemistry* **1989**, *28* (19), 7913−7918.
(22) Fujii, K.; Yasaka, Y.; Ueno, M.; Koyanagi, Y.; Kasuga, S.; Matano, Y.; Kimura, Y. Excited-State Proton Transfer of Cyanonaphthols in Protic Ionic Liquids: Appearance of a New Fluorescent Species. *J. Phys. Chem. B* **2017**, *121* (24), 6042−6049.
(23) Sebök-Nagy, K.; Biczók, L.; Morimoto, A.; Shimada, T.; Inoue, H. Energy Dissipation Processes of Singlet-Excited 1-Hydroxyfluorenone and its Hydrogen-bonded Complex with N-methylimidazole. *Photochem. Photobiol.* **2004**, *80* (1), 119−126.
(24) Spry, D. B.; Goun, A.; Bell, C. B.; Fayer, M. D. Identification and Properties of the 1La and 1Lb States of Pyranine (HPTS). *J. Chem. Phys.* **2006**, *125*, 144514.
(25) Vasak, M.; Whipple, M. R.; Berg, A.; Michl, J. Magnetic Circular Dichroism of Cyclic pi-Electron Systems. 13. Derivatives of Pyrene. *J. Am. Chem. Soc.* **1978**, *100* (22), 6872−6877.
(26) Wirth, P.; Schneider, S.; Dörr, F. S1-Lifetimes of Triphenylmethane and Indigo Dyes Determined by the Two-Photon-Fluorescence Technique. *Opt. Commun.* **1977**, *20* (1), 155−158.
(27) Fox, T.; Kollman, P. A. Application of the RESP Methodology in the Parametrization of Organic Solvents. *J. Phys. Chem. B* **1998**, *102* (41), 8070−8079.
(28) Wang, J.; Wolf, R. M.; Caldwell, J. W.; Kollman, P. A.; Case, D. A. Development and Testing of a General Amber Force Field. *J. Comput. Chem.* **2004**, *25* (9), 1157−1174.
(29) Huige, C. J. M.; Altona, C. Force Field Parameters for Sulfates and Sulfamates Based on Ab Initio Calculations: Extensions of AMBER and CHARMM Fields. *J. Comput. Chem.* **1995**, *16* (1), 56−79.
(30) Case, D. A.; Babin, V.; Berryman, J. T.; Betz, R. M.; Cai, Q.; Cerutti, D. S.; Cheatham, T. E., III; Darden, T. A.; Duke, R. E.; Gohlke, H.; et al. *The Amber Molecular Dynamics Package*; University of California: San Francisco, 2014.
(31) Salomon-Ferrer, R.; Götz, A. W.; Poole, D.; Le Grand, S.; Walker, R. C. Routine Microsecond Molecular Dynamics Simulations with AMBER on GPUs. 2. Explicit Solvent Particle Mesh Ewald. *J. Chem. Theory Comput.* **2013**, *9* (9), 3878−3888.
(32) Loncharich, R. J.; Brooks, B. R.; Pastor, R. W. Langevin Dynamics of Peptides: The Frictional Dependence of Isomerization Rates of N-acetylalanyl-N′-methylamide. *Biopolymers* **1992**, *32* (5), 523−535.
(33) Titov, A. V.; Ufimtsev, I. S.; Luehr, N.; Martinez, T. J. Generating Efficient Quantum Chemistry Codes for Novel Architectures. *J. Chem. Theory Comput.* **2013**, *9* (1), 213−21.
(34) Isborn, C. M.; Luehr, N.; Ufimtsev, I. S.; Martinez, T. J. Excited-State Electronic Structure with Configuration Interaction Singles and Tamm-Dancoff Time-Dependent Density Functional Theory on Graphical Processing Units. *J. Chem. Theory Comput.* **2011**, *7* (6), 1814−1823.
(35) Eastman, P.; Swails, J.; Chodera, J. D.; McGibbon, R. T.; Zhao, Y.; Beauchamp, K. A.; Wang, L.-P.; Simmonett, A. C.; Harrigan, M. P.; Stern, C. D.; et al. OpenMM 7: Rapid Development of High Performance Algorithms for Molecular Dynamics. *PLoS Comput. Biol.* **2017**, *13* (7), e1005659.
(36) Henkelman, G.; Uberuaga, B. P.; Jonsson, H. A Climbing Image Nudged Elastic Band Method for Finding Saddle Point and Minimum Energy Paths. *J. Chem. Phys.* **2000**, *113*, 9901−9904.
(37) Thomaz, J. E.; Bailey, H. E.; Fayer, M. D. The Influence of Mesoscopic Confinement on the Dynamics of Imidazolium-Based Room Temperature Ionic Liquids in Polyether Sulfone Membranes. *J. Chem. Phys.* **2017**, *147* (19), 194502.
(38) Ito, N.; Arzhantsev, S.; Maroncelli, M. The Probe Dependence of Solvation Dynamics and Rotation in the Ionic Liquid 1-butyl-3-methyl-imidazolium hexafluorophosphate. *Chem. Phys. Lett.* **2004**, *396* (1−3), 83−91.
(39) Koti, A.; Krishna, M.; Periasamy, N. Time-Resolved Area-Normalized Emission Spectroscopy (TRANES): a Novel Method for Confirming Emission From Two Excited States. *J. Phys. Chem. A* **2001**, *105* (10), 1767−1771.

https://dx.doi.org/10.1021/acs.jpcb.0c05525
J. Phys. Chem. B 2020, 124, 7897−7908

(40) Koti, A.; Periasamy, N. Application of Time Resolved Area Normalized Emission Spectroscopy to Multicomponent Systems. *J. Chem. Phys.* **2001**, *115* (15), 7094−7099.
(41) Koti, A.; Periasamy, N. Time Resolved Area Normalized Emission Spectroscopy (TRANES) of DMABN Confirms Emission from Two States. *Res. Chem. Intermed.* **2002**, *28* (7−9), 831−836.
(42) Lawler, C.; Fayer, M. D. Proton Transfer in Ionic and Neutral Reverse Micelles. *J. Phys. Chem. B* **2015**, *119* (19), 6024−6034.
(43) Reid, P. J.; Silva, C.; Barbara, P. F.; Karki, L.; Hupp, J. T. Electronic Coherence, Vibrational Coherence, and Solvent Degrees of Freedom in the Femtosecond Spectroscopy of Mixed-Valence Metal Dimers in H2O and D2O. *J. Phys. Chem.* **1995**, *99* (9), 2609−2616.
(44) Rosenthal, S. J.; Xie, X.; Du, M.; Fleming, G. R. Femtosecond Solvation Dynamics in Acetonitrile: Observation of the Inertial Contribution to the Solvent Response. *J. Chem. Phys.* **1991**, *95* (6), 4715−4718.
(45) Jarzeba, W.; Walker, G. C.; Johnson, A. E.; Kahlow, M. A.; Barbara, P. F. Femtosecond Microscopic Solvation Dynamics of Aqueous Solutions. *J. Phys. Chem.* **1988**, *92* (25), 7039−7041.
(46) Dreuw, A.; Head-Gordon, M. Failure of Time-Dependent Density Functional Theory for Long-Range Charge-Transfer Excited States: The Zincbacteriochlorin-Bacteriochlorin and Bacteriochlorophyll-Spheroidene Complexes. *J. Am. Chem. Soc.* **2004**, *126*, 4007−4016.
(47) Chiariello, M. G.; Rega, N. Exploring Nuclear Photorelaxation of Pyranine in Aqueous Solution: An Integrated Ab Initio Molecular Dynamics and Time-Resolved Vibrational Analysis Approach. *J. Phys. Chem. A* **2018**, *122*, 2884−2893.
(48) Heo, W.; Uddin, N.; Park, J. W.; Rhee, Y. M.; Choi, C. H.; Joo, T. Coherent Intermolecular Proton Transfer in the Acid-Base Reaction of Excited State Pyranine. *Phys. Chem. Chem. Phys.* **2017**, *19*, 18243−18251.
(49) Levine, B. G.; Ko, C.; Quenneville, J.; Martinez, T. J. Conical Intersections and Double Excitations in Time-Dependent Density Functional Theory. *Mol. Phys.* **2006**, *104*, 1039−1051.
(50) Vilčiauskas, L.; Tuckerman, M. E.; Melchior, J. P.; Bester, G.; Kreuer, K.-D. First Principles Molecular Dynamics Study of Proton Dynamics and Transport in Phosphoric Acid/Imidazole (2:1) System. *Solid State Ionics* **2013**, *252*, 34−39.

https://dx.doi.org/10.1021/acs.jpcb.0c05525
J. Phys. Chem. B 2020, 124, 7897−7908